J Adv Ceram

Research Article

Regulating the composition, structure, and nanoscale dimensions of $Yb_2Si_2O_7$ environmental barrier coating to achieve a biomimetic teakwood-like functional structure by waste gas recycling

Jungui Zhang[1,2], Guifang Han[1,✉], Xinxin Cao[1], Xiaofeng Zhang[2,✉], Jingde Zhang[1], Min Liu[2], Kesong Zhou[2]

Cite this article: Zhang J, Han G, Cao X, et al. *J Adv Ceram* 2025, **14**(2): 9221021. https://doi.org/10.26599/JAC.2024.9221021

ABSTRACT: The unique multilayer, multiscale structure of teakwood results in excellent mechanical and long-term environmental stability, providing inspiration for the biomimetic design of environmental barrier coating (EBC) structures. However, achieving the desired biomimetic structure control in high-temperature plasma spraying is a challenging task that requires new technological breakthroughs. In this study, a multiscale nano $Yb_2Si_2O_7$–Yb_2SiO_5 (YbDS–YbMS) composite EBC with a teakwood-like lamellar structure was realized via a novel alternating vapor/liquid phase deposition method involving plasma spraying-physical vapor deposition (PS-PVD). Volatilized waste SiO_2 from $Yb_2Si_2O_7$ (YbDS) was reused and deposited on the coating surface during the spraying process, where a regularly arranged multilayer structure was formed in the coating by the alternate deposition of gaseous SiO_2 and droplet YbDS. In addition, SiO_2 on the coated surface formed nanoclusters and dome-shaped nanocrystals via homogeneous and heterogeneous nucleation, respectively, and some of them gradually formed a continuous nanofilm as the arc current increased. The deposited SiO_2 reacted *in situ* with the decomposed phase YbMS in the coating to form YbDS, preserving its multiscale nanostructure after heat treatment and enabling the preparation of the YbDS–YbMS composite coating. This work provides a new design strategy and method for the preparation of coatings using YbDS and other spray powders with similar decomposition and volatilization characteristics during the plasma spraying process.

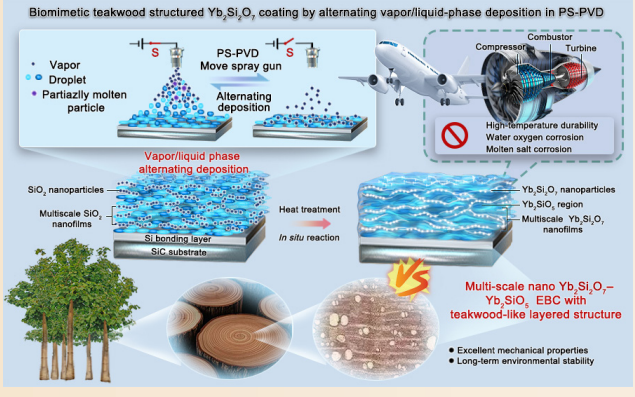

KEYWORDS: teakwood-like lamellar structure; alternating vapor/liquid phase deposition; nanofilm; $Yb_2Si_2O_7$–Yb_2SiO_5 (YbDS–YbMS) composite coating; environmental barrier coating (EBC)

1 Introduction

SiC-based ceramic matrix composites (SiC–CMCs) have been widely investigated as ideal candidates for high-temperature applications in gas turbine engines owing to their low density, excellent high-temperature mechanical properties, and good thermomechanical stability [1,2]. Furthermore, a passivating SiO_2 surface layer forms on SiC under dry air oxidization conditions, which enhances the oxidation resistance of SiC [3]. However, the SiO_2 scale easily reacts with water vapor to form volatile $Si(OH)_4$ gases in high-temperature steam combustion environments, which significantly compromises the service life of CMC_S [4–6]. Therefore, it is essential to prepare environmental barrier coatings (EBCs) on the surface of CMCs to protect them from rapid recessions in harsh combustion environments [7–11].

Advanced structural materials inspired by natural biological materials are expected to become the next generation of engineering materials [12–15]. Teakwood is appreciated for its high mechanical strength, excellent corrosion resistance, good dimensional stability, and natural durability [16–18]. It is commonly used in luxury yachts, royal palaces, high-end furniture, and wooden bridges (Fig. 1(a)), such as the deck of the

[1] Key Laboratory for Liquid-Solid Structural Evolution and Processing of Materials (Ministry of Education), School of Materials Science and Engineering, Shandong University, Jinan 250061, China. [2] National Engineering Laboratory for Modern Materials Surface Engineering Technology & The Key Lab of Guangdong for Modern Surface Engineering Technology & Guangdong-Hong Kong Joint Laboratory of Modern Surface Engineering Technology, Institute of New Materials, Guangdong Academy of Sciences, Guangzhou 510650, China.

✉ Corresponding authors. E-mail: G. Han, gfhan@sdu.edu.cn; X. Zhang, zxf200808@126.com

Received: August 15, 2024; Revised: November 13, 2024; Accepted: December 18, 2024

Fig. 1 (a) Application scenarios and (b) microstructure of teakwood.

Titanic [19], Thailand's Vimanmek Mansion Palace, and Myanmar's century-old U Bein Bridge. Surprisingly, the teakwood salvaged from the Titanic has withstood more than a century of seawater corrosion and remains completely intact [20]. By revealing the internal structure of the teakwood, as shown in Fig. 1(b), we discovered that the cross-section of the teak exhibited a regularly arranged lamellar structure composed of hierarchical film-to-bulk heterogeneous biphasic materials.

Moreover, lamellar coatings with thin films and nanostructures exhibit excellent mechanical properties, such as strength [21,22], stiffness [22,23], toughness [21,22,24], and fatigue resistance [25], as well as gas barrier properties [24,26,27]. This provides us with a good approach for designing and preparing high-performance EBC, which may have excellent thermomechanical properties and outstanding resistance to steam corrosion. In recent years, rare-earth silicates, especially ytterbium monosilicate (Yb_2SiO_5, referred to as YbMS) and disilicate ($Yb_2Si_2O_7$, referred to as YbDS), have been extensively reported and considered to be among the most promising EBC materials due to their low thermal conductivity, good phase stability in high-temperature water vapor environments, and relatively comparable coefficients of thermal expansion (CTEs) with those of SiC–CMCs [28–32]. YbDS exhibits higher fracture toughness and a lower CTE, which is more compatible with that of CMC_S, whereas YbMS shows better resistance to high-temperature water vapor corrosion [33,34]. The combination of these two materials has been shown to enhance the performance of EBCs, as demonstrated by the work of Chen *et al.* [35], who developed a trilayer EBC system consisting of a SiC inner layer, a Si bond layer and mixed YbDS–YbMS topcoats. They reported that a mixed topcoat with 60 wt% YbDS and 40 wt% YbMS showed superior water vapor corrosion resistance, effectively protecting the substrate from damage even after exposure at 1500 °C for 20 h. Additionally, the study by Garcia *et al.* [36] focused on the characterization of YbDS–YbMS composite EBCs produced through in situ plasma spray processing, revealing the phase evolution and thermomechanical stability of these coatings. Their work highlighted the benefits of monosilicate phase evolution for crack healing during high-temperature exposure. Furthermore, research by Yu *et al.* [37] presented a gradient EBC design, which leveraged the advantages of both YbMS and YbDS to achieve excellent resistance to water vapor corrosion and minimal thermally grown oxide (TGO) layer thickness after exposure at 1300 °C for 100 h. Therefore, the development of a multiscale nano dual-phase YbDS–YbMS composite EBC with a teakwood-like hierarchical structure was proposed to obtain excellent resistance to steam corrosion along with thermomechanical properties. This requires the synchronous regulation of the composition, structure, and nanoscale dimensions of the coating.

Plasma spray-physical vapor deposition (PS-PVD) technology integrates the features of plasma spraying and physical vapor deposition [38], bridging the gap between traditional thermal spraying and vapor deposition, and provides a variety of coating microstructures composed of gaseous, liquid, and solid deposition units [39,40]. Wu *et al.* [41] obtained a lamellar-structured YbDS–YbMS composite coating through liquid-phase deposition of YbDS molten droplets by PS-PVD. The preferential evaporation of SiO_2 leads to a deviation from the stoichiometric composition of the YbDS feedstock as it traverses the high-temperature plasma plume [42], resulting in the presence of YbMS in the coatings. However, this method results in a random and uncontrollable distribution of YbDS and YbMS phases inside coatings without forming a regular lamellar arrangement similar to the structure of teakwood, nor does it form nanostructures. Wang *et al.* [43] used the PS-PVD process under high-power conditions to prepare a YbDS coating with a quasi columnar structure through the codeposition of vapor phases and incompletely evaporated YbDS droplets. Additionally, nanosized particles were found in the wedge-shaped column during vapor deposition. Hence, the development of an innovative preparation approach is essential to synergistically regulate the composition, structure, and nanoscale dimensions of the coating.

Inspired by the lamellar structures formed by the liquid-phase deposition of YbDS droplets and the nanostructures formed by vapor-phase deposition during the PS-PVD spraying process, the method of vapor/liquid phase interval deposition to regulate the lamellar structure and nanoscale dimensions of YbDS coatings was proposed for the first time in this study. The recovery/redeposition of waste gas (SiO_2) volatilized from molten YbDS droplets via the PS-PVD technique and the control of its morphology via the regulation of the arc current are presented for the first time. Coatings with regularly arranged lamellar nanostructures can be obtained by alternating deposition of SiO_2 gas and liquid phases of molten YbDS droplets via simple movement of the spray gun. Finally, a multiscale nano YbDS–YbMS composite EBC with teakwood-like lamellar structures could be realized on the deposited coatings after heat treatment. The variations in the phase composition and microstructure of the as-deposited (AD) and heat-treated (HT) YbDS coatings with changes in the arc current were studied, and the relevant mechanisms of coating deposition were analyzed in detail. This study offers a new perspective and approach for

coating preparation by plasma spraying using YbDS and powders with similar characteristics of high-temperature decomposition and volatilization, which has significant practical guidance value.

2 Experimental

2.1 EBC preparation

Agglomerated YbDS powders used for EBC were purchased from the Rare Metal Research Institute of the Guangdong Academy of Sciences, China. The sample contained a small amount of YbMS, accounting for approximately 3.1% by weight, as calculated with Jade9 software, and the particle sizes ranged from 5 to 35 μm (Fig. 2). The feedstock Si powders for bonding coating were purchased from Shenzhen Lite New Material Technology Co., Ltd., China. SiC bars (25 mm × 7 mm × 5 mm, Shenzhen Dachuan Ceramic Technology Co., Ltd., China) were used as substrates. The substrate surface was roughened by blasting with 64# alumina solid particles at an air pressure of 0.3 MPa to increase the mechanical locking force between the coating and SiC substrate. The surface roughness of the roughened SiC substrate was ~2.5 μm. The Si/YbDS double-layer EBC was then prepared via a PS-PVD facility (Sulzer-Metco Multicoat, Switzerland) with the spray parameters detailed inTable 1. As the spraying current increased, the spraying power correspondingly increased. A schematic diagram of the YbDS coating process is shown in Fig. 3. After each spraying pass, the spray gun was moved away from the coating surface until the coating temperature dropped to the preheating temperature of 450 °C before the next spraying pass was applied, which made it possible for the vaporized silicon-containing substances to be redeposited back to the coating surface during the waiting period. The process was repeated to achieve alternating deposition of the coating in vapor/liquid phases. The as-deposited YbDS coating was heat-treated at 1300 °C under Ar for 25 h with heating and cooling rates of 5 °C/min to eliminate amorphous phases.

2.2 EBC characterizations

The phase compositions of the AD and HT YbDS coatings were

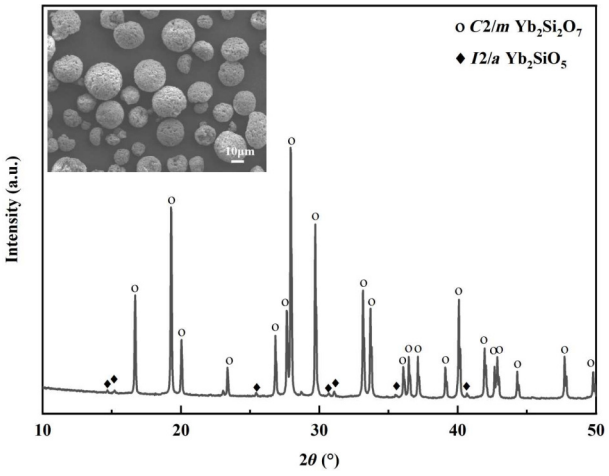

Fig. 2 XRD pattern and micrograph of agglomerated YbDS feedstock powders.

Table 1 PS-PVD operating parameters used in this study

PS-PVD layer	Current (A)	Ar (NLPM)	H_2 (NLPM)	Power (kW)	Feeding rate (g/min)	Preheating temperature (°C)	Spray distance (mm)	Number of spray passes	Chamber pressure (mbar)
Si	1650	110	6	50.1	10.8	700	450	28	40
YbDS	1450	110	6	42.6	4.5	450	450	80	40
	1600	110	6	47.7	4.5	450	450	80	40
	1650	110	6	51.7	4.5	450	450	80	40
	1700	110	6	56.9	4.5	450	450	80	40

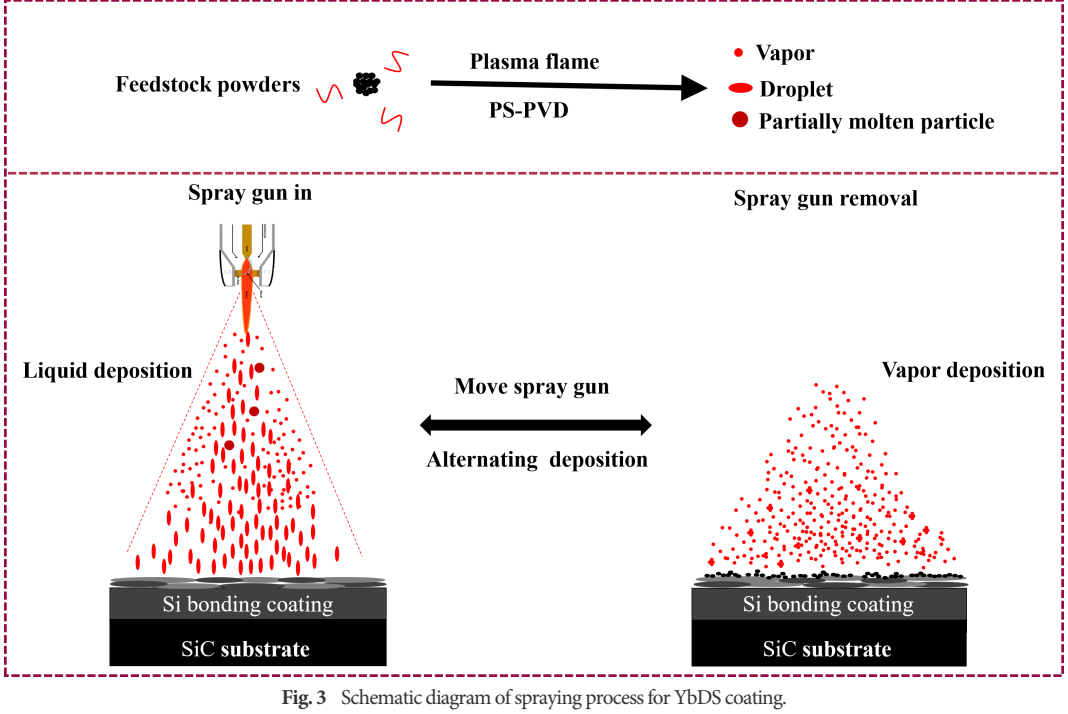

Fig. 3 Schematic diagram of spraying process for YbDS coating.

identified via an X-ray diffractometer (XRD; 10°–70°, a step of 0.02°, scanning speed of 2 (°)/min, D8-Advance, Bruker, Germany). The crystallinity of the coating was determined via the relative crystallinity calculation method, which employs Jade9 software to calculate the ratio of the crystalline peak area to the combined area of the crystalline peaks and amorphous regions for each sample [44]. The reference intensity ratio (RIR) method [45] was used to quantify the content of each phase in the YbDS powders and HT-YbDS coating. The microstructures of the coatings were characterized via a field emission-scanning electron microscope (FE-SEM; Nova-Nono450, FEI, USA) in secondary electron (SE) and backscattered electron (BSE) imaging modes, and the proportions of the elements were analyzed via an energy dispersive X-ray spectroscope (EDS; Oxford INCAx-sight 6427, Oxford Instruments, UK). The distribution of elements was analyzed via an electron probe X-ray microanalyzer (EPMA; JXA-8100, JEOL, Japan). The surface roughness of the substrate after abrasive blasting was characterized via a 3D profilometer (Dektak XT, Bruker, Germany).

3 Results and discussion

3.1 Phase evolution with the plasma arc current

The XRD patterns of the AD and HT-YbDS coatings at different plasma arc currents are shown in Fig. 4. The crystallinities of the AD-YbDS coatings are listed in Table 2. Two very distinct broad humps (2θ ranges of 24°–38° and 40°–70°) are present in the AD-YbDS coating (Fig. 4(a)), indicating that the coating was predominantly amorphous, which is consistent with the low crystallinity of these materials listed in Table 2. Its crystallinity decreases monotonically with increasing arc current. Moreover, the Yb_2O_3, metastable *P*21/*c* YbMS and stable *I*2/*a* YbMS phases are observed in all the AD-YbDS coatings, whereas a small amount of the YbDS phase is present only in the AD-YbDS-1450A and AD-YbDS-1600A coatings. It was reported that the metastable phase *P*21/*c* YbMS transformed into the stable *I*2/*a* YbMS phase after heat treatment [42,44,46]. The amorphous feature of AD-YbDS coatings is deemed to be the result of rapid cooling of molten silicate droplets during the plasma spraying process [46,47]. During the plasma spraying process, the higher partial vapor pressure of SiO than of Yb leads to substantial Si species loss from the originally stoichiometric YbDS powders, resulting in the formation of the Yb_2O_3 and YbMS phases [42]. With increasing arc current and spray power, the plasma temperature increases, which leads to complete melting of the YbDS powders and volatilization of Si-species substances, resulting in the gradual disappearance of the YbDS phase in the AD-YbDS coatings. Simultaneously, the rapid solidification of the newly added droplets further enhances the degree of amorphization in the AD-YbDS coating.

The EBC system should be crystalline and stable to protect the substrate from steam corrosion when exposed to high-temperature combustion environments. Therefore, heat treatment of AD-YbDS coatings is necessary in this study, and the XRD patterns of the HT-YbDS coatings are shown in Fig. 4(b). After annealing, the two broad humps (Fig. 4(a)) disappeared, indicating that the HT-YbDS coatings were completely crystallized, which is consistent with their high crystallinity, as listed in Table 2. This result was attributed mainly to the longer duration of heat treatment used in the experiment. Unlike the AD-YbDS coating, only the *C*2/*m* YbDS and *I*2/*a* YbMS phases are observed in the HT-YbDS coating. The absence of Yb_2O_3 in the AD-YbDS coatings after heat treatment is related mainly to the reaction of Yb_2O_3 with SiO_2 to form YbMS and/or YbDS. Additionally, the metastable *P*21/*c* YbMS phase in the AD-YbDS coating gradually transforms into its isomorphic stable *I*2/*a* YbMS phase after treatment. The content of each phase in the YbDS powders and HT-YbDS coating is listed in Table 3. A significant proportion of YbMS is present in all the HT-YbDS coatings because of the loss of Si–O during the plasma spraying process. Surprisingly, the mass fraction of the YbMS phase increases from 63.9% to 75.8% and then continuously decreases with increasing arc current from 1450 to 1700 A. The opposite trend is found for the YbDS phase. These findings indicate that with increasing current, bidirectional regulation of the YbMS component in the YbDS coating is achieved. However, other studies have reported a monotonic increase in the amount of YbMS with increasing spray power [46,48]. This seemingly abnormal phenomenon is attributed mainly to the unique deposition method used in this study, i.e., vapor/liquid phase interval deposition, which allows some of the volatilized SiO_2 vapor to return to the coating through vapor deposition and will be discussed later.

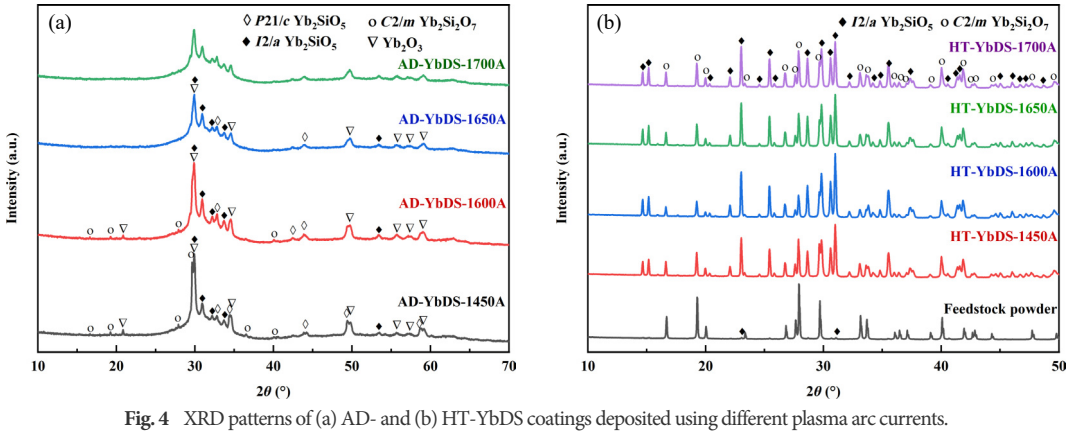

Fig. 4 XRD patterns of (a) AD- and (b) HT-YbDS coatings deposited using different plasma arc currents.

Table 2 Calculated crystallinities of AD- and HT-YbDS coatings (Unit: %)

Plasma arc current	Feedstock	AD-YbDS-1450A	AD-YbDS-1600A	AD-YbDS-1650A	AD-YbDS-1700A	HT-YbDS-1450A	HT-YbDS-1600A	HT-YbDS-1650A	HT-YbDS-1700A
Crystallinity	99.0	35.4	33.2	29.8	23.4	99.3	99.1	99.2	99.0

3.2 Microstructure evolution after annealing

BSE SEM cross-section micrographs of the AD and HT-YbDS coatings at different plasma arc currents are shown in Fig. 5. All the AD-YbDS coatings exhibited a lamellar stacking pattern (Fig. 5(a)). A small number of partially melted particles exist in the AD-YbDS-1450A and AD-YbDS-1600A coatings, which gradually disappear as the deposition power increases. This is attributed to the high-temperature plasma stream of the PS-PVD technology, which effectively melts the YbDS powders. The low viscosity of these melted particles allows them to spread effectively and stack on top of each other, thus avoiding the reticulation cracks produced by APS technology [46,48]. However, all AD-YbDS coatings, except for the AD-YbDS-1700A coating, showed vertical cracks, which could be attributed to the mismatch in the CTE of the coating during the cooling process, resulting in tensile stress. Once the accumulated tensile stress exceeds the tensile strength of the coating, longitudinal vertical cracking occurs [49]. In addition, all AD-YbDS coatings show areas of varying contrast due to phase separation, with relatively brighter areas corresponding to Si-depleted regions. The chemical compositions of the samples were detected via EDS and are listed in Table 4.

Table 3 Summary of phase fraction analysis for heat-treated YbDS coatings (Unit: wt%)

Sample	Feedstock	HT-YbDS-1450A	HT-YbDS-1600A	HT-YbDS-1650A	HT-YbDS-1700A
YbDS	96.9	36.1	24.2	37.3	41.8
YbMS	3.1	63.9	75.8	62.7	58.2

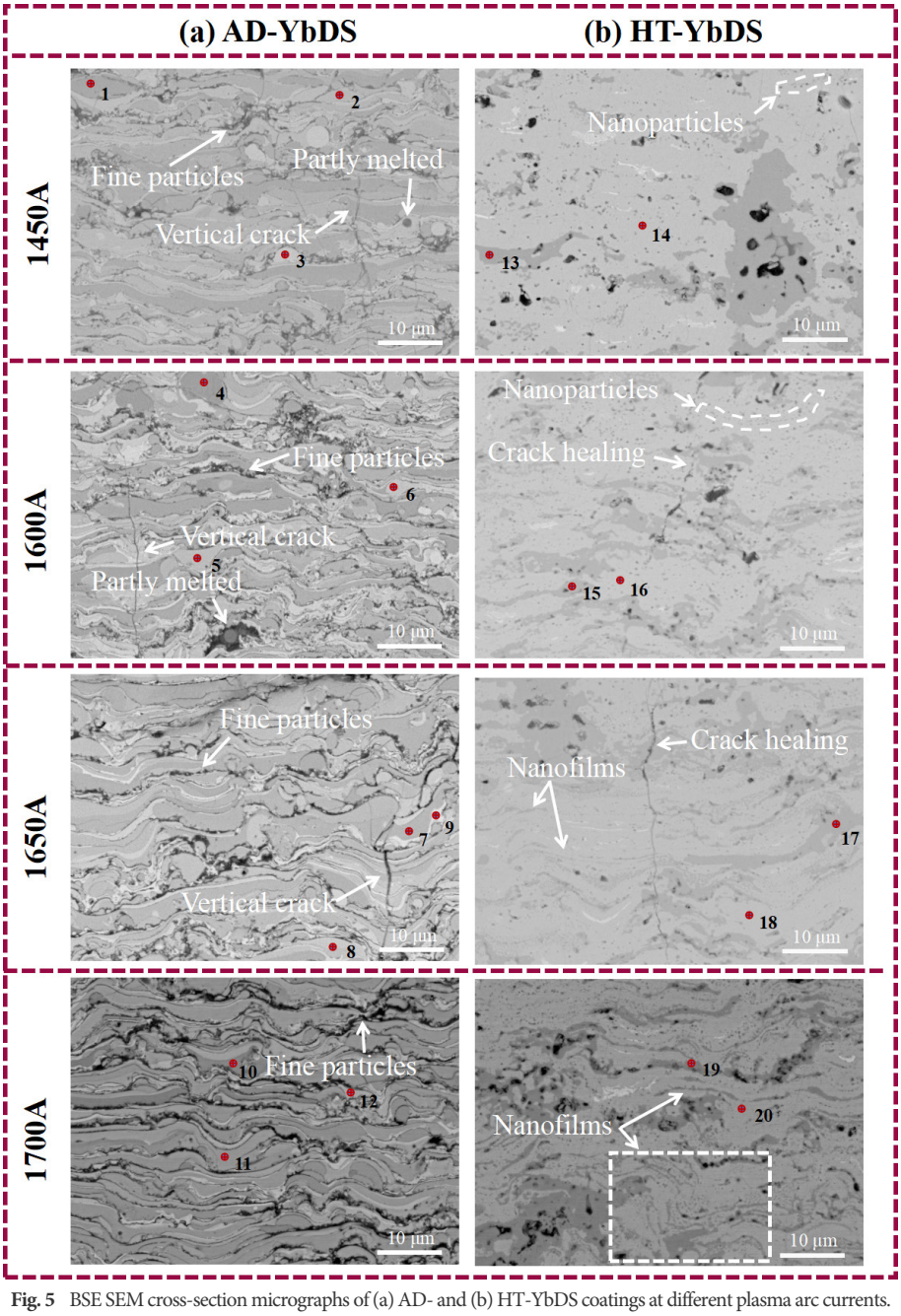

Fig. 5 BSE SEM cross-section micrographs of (a) AD- and (b) HT-YbDS coatings at different plasma arc currents.

Notably, black fine particles were observed in the interlayer gap of the AD-YbDS coating. As the deposition power increases, the number of these black fine particles increases. For the AD-YbDS-1650A and AD-YbDS-1700A coatings, some of the black particles gradually formed a continuous film. To accurately determine the chemical composition of the black particles, an EPMA mapping scan of O, Si, and Yb in the cross-section of the AD-YbDS-1700A coating was carried out, as shown in Fig. 6. The scan analysis revealed notably higher concentrations of Si and O within the regions where black particles were present, whereas the concentration of Yb was lower. This suggests that the black particles are predominantly composed of SiO_2, further confirming that vapor deposition of SiO_2 occurred during the spraying process. Moreover, the black fine particles (SiO_2) in the AD-YbDS coating are distributed in a wavy pattern along the horizontal direction of the coating and are arranged at intervals in the vertical direction, which is related to the unique spraying process used in this study. As shown in Fig. 3, when the spray gun is directly facing the coating surface for spraying, liquid droplet deposition mainly occurs. However, when the spray gun is moved away from the coating surface, the vaporized SiO_2, which is free from droplet interference, begins to deposit on the coating surface, and this vapor phase deposition dominates. The black fine particles observed at regular intervals are likely due to this gas deposition. Alternating liquid/vapor phase deposition is thus achieved by repeatedly moving the gun in and out. Moreover, these fine particles were conformally formed along the wave-like surface of the coatings.

Table 4 EDS compositions (at%) of locations indicated in Fig. 5 by the numbers

Spot	Yb (at%)	Si (at%)	O (at%)	Yb/Si
1	39.1	23.9	37.0	1.64
2	25.5	12.5	62.0	2.04
3	45.5	17.7	36.8	2.57
4	22.9	13.1	64.0	1.75
5	24.9	12.7	62.4	1.96
6	26.0	11.4	62.6	2.28
7	23.5	19.1	57.4	1.23
8	28.5	14.6	56.9	1.95
9	32.1	11.2	56.7	2.87
10	27.7	24.8	47.5	1.12
11	32.0	22.1	45.9	1.45
12	36.3	17.6	46.1	2.06
13	23.4	21.8	54.8	1.07
14	31.4	15.5	53.1	2.03
15	25.4	24.5	50.1	1.04
16	33.1	16.9	50.0	1.96
17	26.3	26.1	47.6	1.01
18	36.0	18.2	45.8	1.98
19	25.8	24.8	49.4	1.04
20	31.3	15.9	52.8	1.97

The microstructures of the HT-YbDS coatings produced with different fabrication parameters are shown in Fig. 5(b). Compared with those of the AD-YbDS coatings, the clear outline of the interlayer disappeared, and the width of the cracks narrowed. These changes are attributed mainly to the diffusion of atoms, phase transformations, grain growth, and the reduction in surface energy during the heat treatment process [50–53]. All the HT-YbDS coatings exhibited two main contrast regions, gray and dark gray, which were less intense than the regions of the as-deposited

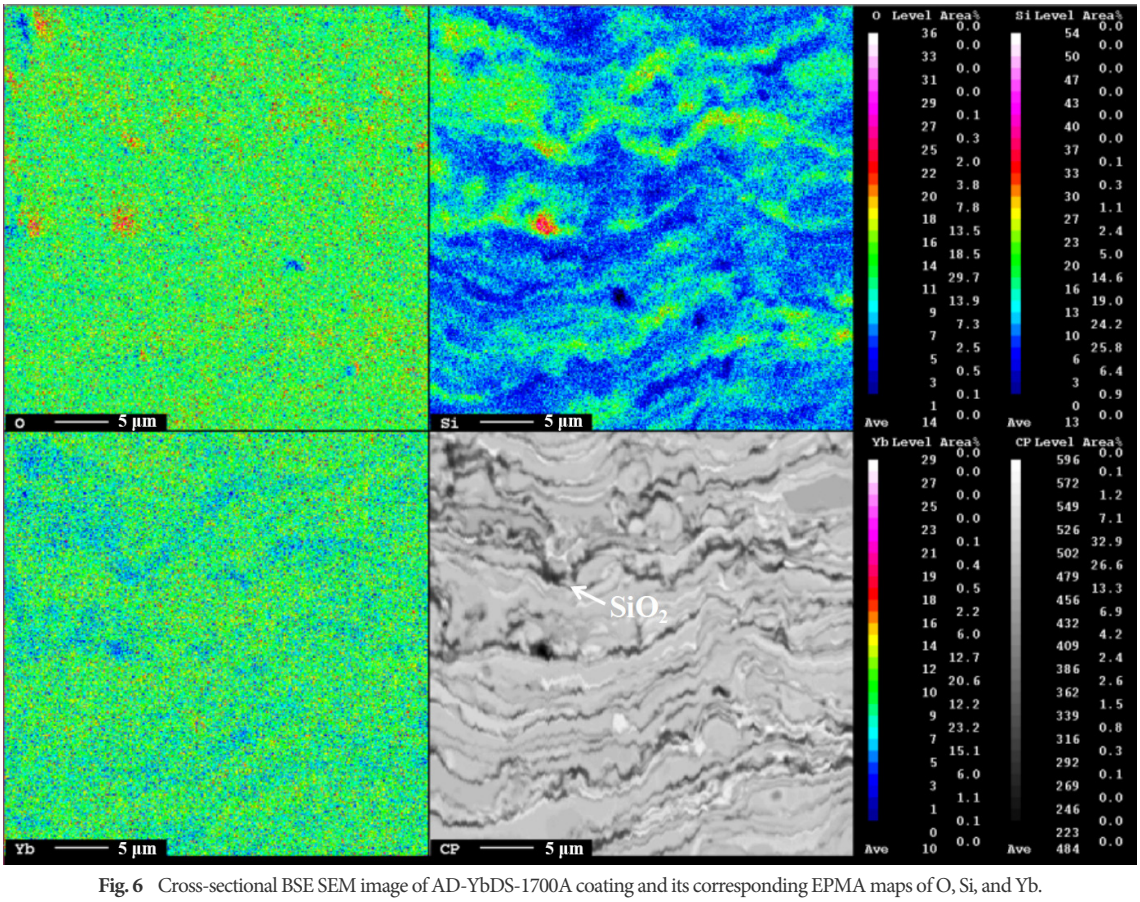

Fig. 6 Cross-sectional BSE SEM image of AD-YbDS-1700A coating and its corresponding EPMA maps of O, Si, and Yb.

coatings. The chemical compositions of the samples were detected via EDS and are listed in Table 4. The molar ratios of Yb/Si for spots 13, 15, 17, and 19 (dark gray) and spots 14, 16, 18, and 20 (gray) are close to those of YbDS and YbMS, respectively, which is consistent with the XRD analysis results shown in Fig. 4(b). All the HT-YbDS coatings display a morphology with YbMS as the main phase and YbDS as the secondary phase. Notably, the black fine particles (SiO_2) in the AD-YbDS coatings disappeared after heat treatment. Combined with the EDS and XRD results, these results suggest that SiO_2 reacts with the decomposed phase YbMS to form YbDS. In addition, several nanoscale YbDS particles were found in the HT-YbDS-1450A coating. Its number increases gradually with increasing deposition power until a thin YbDS film is formed. Therefore, the vapor-deposited black fine particles (SiO_2) react *in situ* with the decomposed YbMS to form YbDS nanoparticles or nanofilms between two passes of spraying after heat treatment. To observe the morphology in detail, magnified SEM images are shown in Fig. 7 for the AD-YbDS and HT-YbDS coatings at different plasma arc currents. Within the AD-YbDS coatings, the deposited SiO_2 particles reached the nanoscale. As the spraying current increased, these nanoscale SiO_2 particles gradually accumulated, eventually forming a continuous short-range nanofilm. Similarly, in the HT-YbDS coatings, the YbDS nanoparticles also exhibited similar accumulation and film formation processes. Particularly in the HT-YbDS-1700A coating, the formation of nanoparticles and nanofilms was particularly evident and clearly observed. This is a regular lamellar structure with YbMS as the dominant phase and embedded YbDS nanoparticles/nanofilms, i.e., a multiscale nano YbDS–YbMS composite coating with a structure similar to that of teakwood.

Two representative surface morphologies, nanograins, and clusters, are observed (Fig. 8) for sample AD-YbDS-1700A, whose

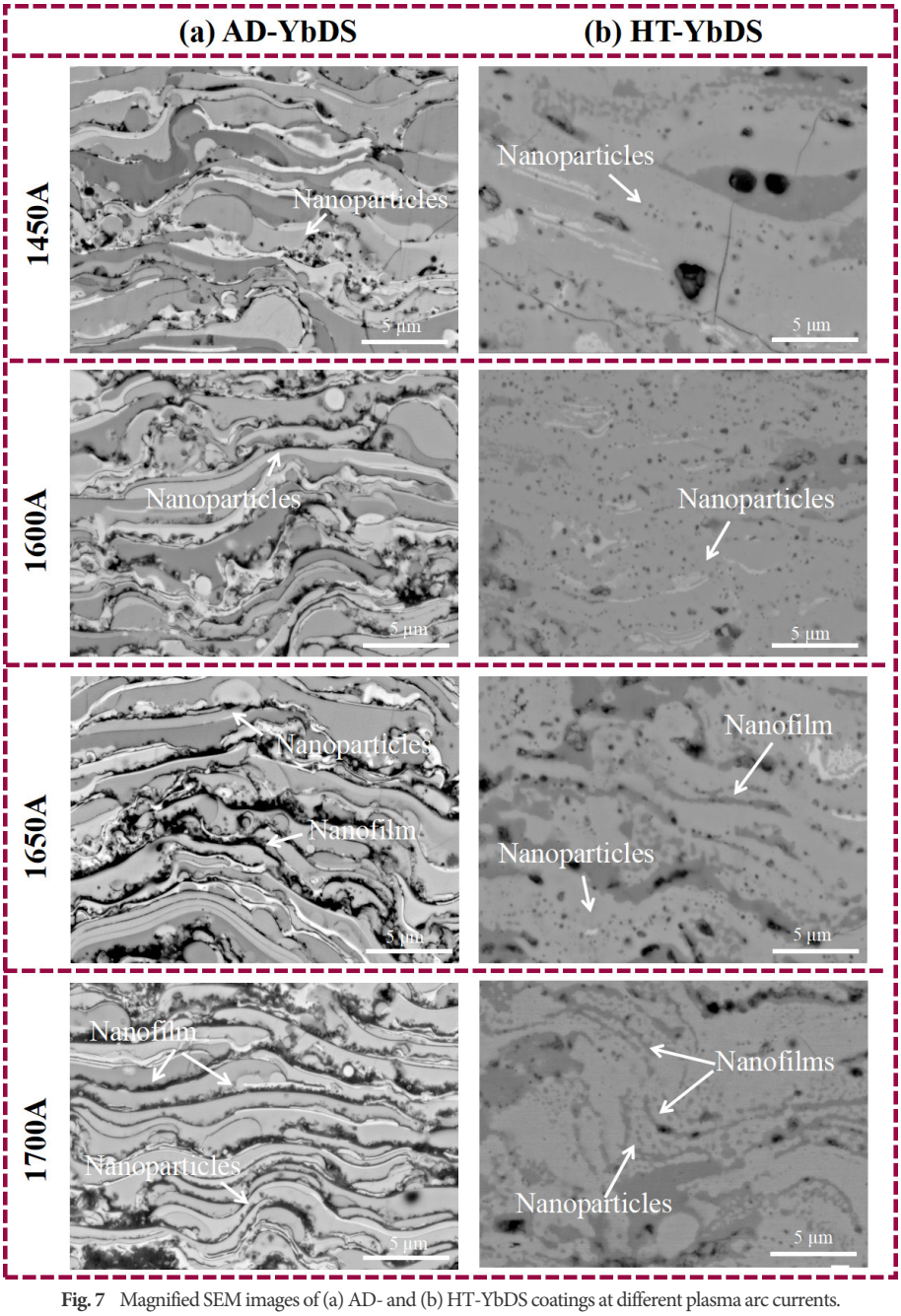

Fig. 7 Magnified SEM images of (a) AD- and (b) HT-YbDS coatings at different plasma arc currents.

清華大学出版社 Tsinghua University Press | SciOpen

sizes are much smaller than those of the feedstock powders. These morphologies are closely correlated with SiO_2 vapor phase deposition. In the following section, the formation mechanism is discussed in detail from both thermodynamic and crystal growth dynamic aspects.

3.3 Thermodynamic conditions for coating deposition

A schematic of the formation of a multiscale nano YbDS–YbMS composite coating with a teakwood-like structure is shown in Fig. 9, which is based on the above analysis of its phase composition and microstructure. The key to obtaining this unique structure is controlling the evaporation and condensation of SiO_2. Therefore, exploring the underlying mechanism is crucial.

The vapor phase deposition process of SiO_2 involves two fundamental steps: First, the sprayed powders are heated and decomposed in a high-temperature plasma flame, leading to the evaporation of SiO_2; second, the evaporated SiO_2 gas condenses on the cooled coating surface. Its vapor pressure varies with temperature thermodynamically according to the Clausius–Clapeyron equation as Eq. (1):

$$\ln p = -\frac{\Delta H}{RT} + C \tag{1}$$

where p is the vapor pressure of the gaseous substance, ΔH is the enthalpy of vaporization, R is the ideal gas constant, T is the temperature in Kelvin, and C is a constant related to the properties of the materials. The temperature of the evaporation source, which is high or low, clearly changes the value of the vapor pressure, which directly affects the evaporation rate of the materials. Additionally, the evaporation and condensation of the materials must satisfy the following thermodynamic conditions (Eq. (2)):

$$\Delta G = nRT \ln \frac{P_0}{P_e} \tag{2}$$

where ΔG represents the Gibbs free energy, n represents the amount of the gas, P_0 represents the actual pressure, and P_e represents the saturation vapor pressure. When $P_0 < P_e$, $\Delta G < 0$, the evaporation process can proceed, whereas when $P_0 > P_e$, $\Delta G > 0$, the condensation process can take place. Under the same external atmospheric pressure and temperature conditions, the vapor pressure of Si-containing substances in YbDS powders is much greater than that of Yb-containing substances [42], increasing their volatility. This is the fundamental reason for the loss of Si in YbDS powders during the plasma spraying process.

According to Eqs. (1) and (2), compared with traditional APS spraying technology, PS-PVD spraying technology has a higher plasma flame temperature, which results in a higher vapor pressure of Si-containing substances in the YbDS powders. Additionally, the lower chamber pressure environment (40 mbar) during spraying greatly promoted the volatilization of Si-containing substances. This is the main reason why YbMS becomes the primary phase in the HT-YbDS coatings. This approach also provides a prerequisite for experimental control of vapor–liquid phase deposition to prepare multiscale nanocomposite coatings.

In the vapor deposition process, the mean free path λ of the volatilized SiO_2 gas molecules determines whether they can efficiently reach the surface of the coating that needs to be deposited, which is related to the air pressure (Eq. (3)):

$$\lambda = \frac{k_B T}{\sqrt{2}\pi d^2 P} \tag{3}$$

where λ is the mean free path of the gas molecules, k_B is the Boltzmann constant, d is the average diameter of the gas molecules, and P is the gas pressure. λ increases with decreasing pressure (Eq. (3)). The low chamber pressure used in the PS-PVD spraying in this study reduces the number of collisions between SiO_2 gas molecules and residual gas molecules, thereby reducing

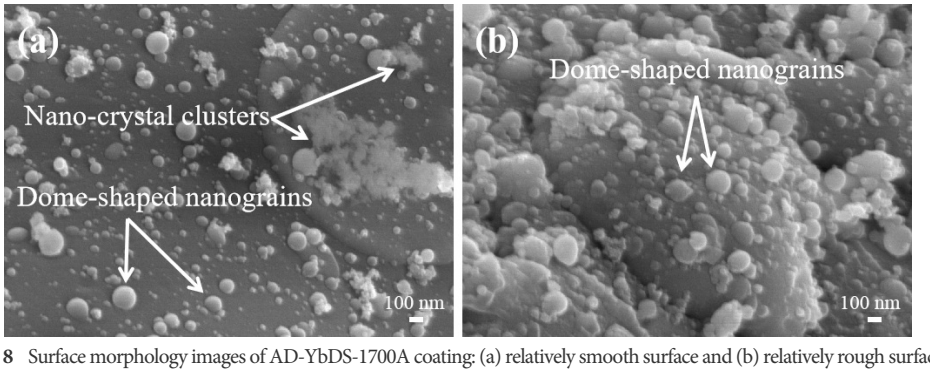

Fig. 8 Surface morphology images of AD-YbDS-1700A coating: (a) relatively smooth surface and (b) relatively rough surface.

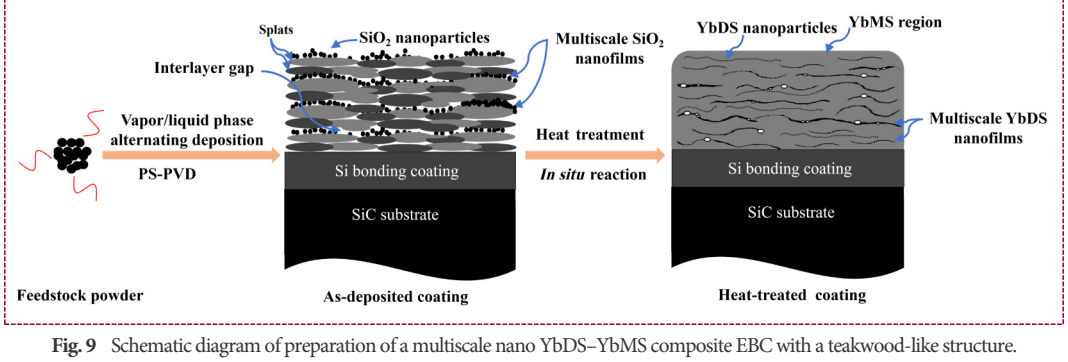

Fig. 9 Schematic diagram of preparation of a multiscale nano YbDS–YbMS composite EBC with a teakwood-like structure.

their scattering effect. This increases λ of the SiO_2 gas molecules, facilitating their arrival at the coating surface for deposition. In contrast, when spraying is conducted in an atmospheric environment, the large scattering effect of air greatly reduces the λ value of the SiO_2 gas molecules, making it difficult for them to reach the coating surface. This is one of the most important reasons why SiO_2 vapor deposition is not easily observed in the APS spraying process of YbDS powders [42,44,46]. Furthermore, when the hot volatilized SiO_2 gas contacts the relatively cold (450 °C) coating surface, it condenses. As the arc current increases, the temperature of the plasma flame increases, which leads to an increase in the vapor pressure of SiO_2. This caused an increased concentration of SiO_2 gas as well as an increased number of SiO_2 particles deposited (Fig. 5(a)).

3.4 Nucleation and growth mechanisms of coating

The thermodynamic conditions for the evaporation and deposition of SiO_2 from molten YbDS droplets could be satisfied by the PS-PVD spraying process. This allows interval deposition of the SiO_2 gas phase and molten YbDS liquid phase by simply moving the spray gun. In addition, as shown in Fig. 9, a lamellar multiscale nanostructure is obtained, the mechanism of which will be discussed in depth based on the nucleation and grain growth modes.

The nucleation mode of vapor-phase condensation can be referred to as liquid-phase solidification, which is divided into homogeneous and heterogeneous nucleation. The critical nucleus size (r^*) for both types of nucleation is related to the degree of undercooling ΔT, and the expressions are shown in Eq. (4):

$$r^* = \frac{2\sigma T_m}{L_m \Delta T} \tag{4}$$

where σ is the specific surface energy, T_m is the equilibrium freezing temperature, and L_m is the latent heat of fusion. Equation (4) shows that the critical nucleus radius is determined by the degree of undercooling. The greater the degree of undercooling, the smaller the critical nucleus radius, making it easier to form a stable nucleus. When the PS-PVD gun is moved away from the coating surface, the interference of the droplets and the effect of the high-temperature plasma plume are eliminated. A large degree of undercooling is established in the vapor phase, and the SiO_2 molecules in the vapor phase rely on energy changes to undergo homogeneous nucleation, forming fine crystalline nuclei. These nuclei then grow into SiO_2 nanocrystals, which aggregate into clustered structures under the influence of surface energy, eventually forming a loose fine-crystal structure on the coating surface (Fig. 8(a)). Similar clustered fine crystals have also been reported in the vapor deposition of 7YSZ thermal barrier coatings by PS-PVD spraying [54]. Furthermore, some SiO_2 molecules in the vapor phase reach the coating surface and undergo heterogeneous nucleation. Compared with homogeneous nucleation, this nucleation method reduces the interfacial energy of nucleation with the aid of these preexisting surfaces, resulting in lower nucleation work. Consequently, nucleation is more likely to take place and grow into dome-shaped nanocrystals, which is also the reason that the dome-shaped nanocrystals in Fig. 8(a) are larger in size than the clustered grains. However, because the thermal energy of the SiO_2 vapor phase dissipates rapidly on the coating surface at relatively lower temperatures, it is difficult for the grains to grow, resulting in most of the grains deposited on the coating surface being nanosized (Fig. 8). The nanostructure formed within the coating benefits from the vapor deposition of the waste gas SiO_2.

To regulate the nanoscale dimensions and structure of the YbDS coating, four different deposition morphologies were prepared under various arc current conditions, as shown in Fig. 7(a). SiO_2 particles first grow into an island-like shape and then into a nanofilm as the current increases, following the three-dimensional growth (Volmer–Weber) model, which is divided into four stages: the nucleation stage, island stage, network stage, and continuous film stage, as shown in Fig. 10. When the arc current is 1450 A, the coating deposition power is relatively low. The volatilization of SiO_2 gas from the feedstock powders is insufficient during the spraying process, resulting in a low concentration of SiO_2 gas within the chamber. This results in a sparse deposition of SiO_2 particles in the AD-YbDS-1450A coating, with the particles being small and dispersed, indicating that this stage is primarily the nucleation stage. When the arc current is 1600 A, the increased deposition power causes more SiO_2 gas to volatilize from the feedstock powders than when the arc current is 1450 A. The concentration of SiO_2 gas in the chamber also increased, allowing the SiO_2 nuclei in the AD-YbDS-1600A coating to gradually aggregate by capturing and adsorbing atoms and growing in three dimensions to form islands. This stage corresponds mainly to the island stage. As the arc current increases to 1650 A, the concentration of SiO_2 gas in the chamber further increases. At this point, the SiO_2 islands in the AD-YbDS-1650A coating meet and merge to form larger islands during the growth process, which then develop into a network-like nanofilm. The nanofilm formed at this stage is short and discontinuous in the length direction, indicating that this stage is mainly the network stage. When the arc current is increased to 1700 A, more SiO_2 gas is volatilized from the feedstock powders during the spraying process, resulting in the highest concentration of SiO_2 gas in the chamber. Consequently, the channels within the network-like nanofilm of the AD-YbDS-1700A coating are filled with newly formed islands, and as these channels gradually fill up, a continuous nanofilm is formed. This stage is mainly the continuous film stage. In the end, a multiscale, multilamellar nanostructure with nanofilms and nanoparticles was formed in the AD-YbDS-1700A coating by alternating vapor/liquid phase deposition. After heat treatment, SiO_2 reacts *in situ* with the decomposed phase of YbMS in the coating to form YbDS. This reaction maintains the morphology of

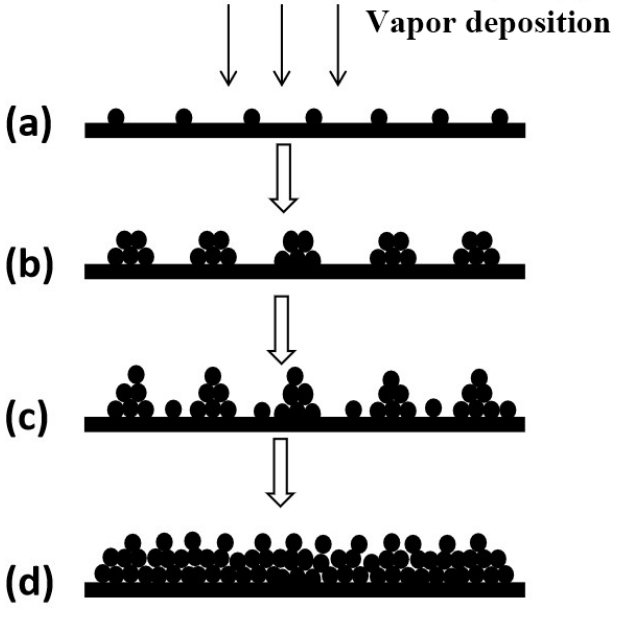

Fig. 10 Schematic diagram of vapor deposition growth of SiO_2 particles in different stages: (a) nucleation stage, (b) island stage, (c) network stage, and (d) continuous film stage.

the SiO_2 vapor deposition, resulting in a stratified structure dominated by the YbMS phase, which is embedded with YbDS nanoparticles/nanofilms, that is, a multiscale nano YbDS–YbMS composite coating with a teakwood-like structure (HT-YbDS-1700A).

4 Conclusions

By utilizing PS-PVD spray technology, effective control of the YbDS coating composition, structure, and nanoscale dimensions was achieved through alternating deposition of vapor/liquid phases by adjusting the arc current. Subsequently, the fabrication of a multiscale nano YbDS–YbMS composite EBC with a teakwood-like lamellar structure was successfully realized with the aid of heat treatment. The following coating deposition mechanisms can be drawn from this work.

(1) In the PS-PVD process, the precise combination of high arc current, low chamber pressure, and low preheating temperature meets the thermodynamic conditions for the evaporation and deposition of SiO_2, resulting in the evaporation of SiO_2 from the powders and its redeposition in the coating. Additionally, the recycled SiO_2 waste gas enables bidirectional regulation of the YbMS component in the YbDS coating, which first increases and then decreases with increasing arc current.

(2) The substantial undercooling effect that occurs as the PS-PVD gun moves away from the coating surface hinders the growth of particles in the SiO_2 vapor deposition process, leading to the formation of nanoparticles. Within this process, homogeneous nucleation results in the formation of nanoclusters, and heterogeneous nucleation gives rise to the creation of dome-shaped nanocrystals on the coating surface, thereby achieving meticulous control over the nanostructure of the coating.

(3) As the arc current gradually increased, the deposition and growth of SiO_2 particles within the coating followed the three-dimensional growth (Volmer–Weber) model. When the arc current reaches 1700 A, some SiO_2 particles deposit and grow into a continuous nanofilm within the coating. Then, representative regularly arranged lamellar multiscale nanostructured YbDS coatings were formed by alternate deposition in the vapor/liquid phases. During the heat treatment process, the deposited SiO_2 reacts *in situ* with the decomposed YbMS phase in the coating to form YbDS, preserving the original deposition morphology of SiO_2 and ultimately resulting in the fabrication of a multiscale nano YbDS–YbMS composite EBC with a teakwood-like lamellar structure.

Research on biomimetic EBCs is scarce, largely due to the challenges of precisely controlling their composition and structure during high-temperature spraying. This study has made breakthroughs in the controlled fabrication of biomimetic teak structure EBCs and has conducted an in-depth analysis of their deposition mechanisms. In our future studies, we will focus on systematically evaluating the corrosion resistance and mechanical properties of these coatings and compare them with findings from the literature.

Acknowledgements

We would like to acknowledge the financial support from the National Natural Science Foundation of China (Nos. 52322104, 52172067, and 92160202), the Natural Science Foundation of Guangdong Province (No. 2021B1515020038), the Guangdong Special Support Program (No. 2019BT02C629), the Guangdong Provincial Science and Technology Program (No. 2023A0505010017), and the Science Center for Gas Turbine Project (No. P2023-C-IV-002-001).

Declaration of competing interest

The authors have no competing interests to declare that are relevant to the content of this article.

References

[1] Song CK, Liu YS, Ye F, *et al.* Enhanced mechanical property and tunable dielectric property of SiC_f/SiC–SiBCN composites by CVI combined with PIP. *J Adv Ceram* 2021, **10**: 758–767.
[2] Zhang JM, Chen XW, Liao CJ, *et al.* Optimizing microstructure and properties of SiC_f/SiC composites prepared by reactive melt infiltration. *J Inorg Mater* 2021, **36**: 1103.
[3] Lee KN. Current status of environmental barrier coatings for Si-based ceramics. *Surf Coat Tech* 2000, **133**: 1–7.
[4] Eaton HE, Linsey GD. Accelerated oxidation of SiC CMC's by water vapor and protection via environmental barrier coating approach. *J Eur Ceram Soc* 2002, **22**: 2741–2747.
[5] Opila EJ. Oxidation and volatilization of silica formers in water vapor. *J Am Ceram Soc* 2003, **86**: 1238–1248.
[6] Li G, Qin L, Cao XQ, *et al.* Water vapor corrosion resistance and failure mechanism of SiC_f/SiC composites completely coated with plasma sprayed tri-layer EBCs. *Ceram Int* 2022, **48**: 7082–7092.
[7] Deijkers JA, Wadley HNG. A duplex bond coat approach to environmental barrier coating systems. *Acta Mater* 2021, **217**: 117167.
[8] Richards BT, Wadley HNG. Plasma spray deposition of tri-layer environmental barrier coatings. *J Eur Ceram Soc* 2014, **34**: 3069–3083.
[9] Lee KN. $Yb_2Si_2O_7$ Environmental barrier coatings with reduced bond coat oxidation rates via chemical modifications for long life. *J Am Ceram Soc* 2019, **102**: 1507–1521.
[10] Lee KN, Miller RA. Development and environmental durability of mullite and mullite/YSZ dual layer coatings for SiC and Si_3N_4 ceramics. *Surf Coat Tech* 1996, **86**: 142–148.
[11] Dong L, Liu MJ, Zhang XF, *et al.* Pressure infiltration of molten aluminum for densification of environmental barrier coatings. *J Adv Ceram* 2022, **11**: 145–157.
[12] Naleway SE, Porter MM, McKittrick J, *et al.* Structural design elements in biological materials: Application to bioinspiration. *Adv Mater* 2015, **27**: 5455–5476.
[13] Wegst UGK, Bai H, Saiz E, *et al.* Bioinspired structural materials. *Nat Mater* 2015, **14**: 23–36.
[14] Chen SM, Gao HL, Sun XH, *et al.* Superior biomimetic nacreous bulk nanocomposites by a multiscale soft-rigid dual-network interfacial design strategy. *Matter* 2019, **1**: 412–427.
[15] Studart AR. Towards high-performance bioinspired composites. *Adv Mater* 2012, **24**: 5024–5044.
[16] Lengowski EC, Bonfatti Júnior EA, Nisgoski S, *et al.* Properties of thermally modified teakwood. *Maderas-Cienc Tecnol* 2021, **23**: 1–16.
[17] Savero AM, Wahyudi I, Rahayu IS, *et al.* Investigating the anatomical and physical-mechanical properties of the 8-year-old superior teakwood planted in muna island, Indonesia. *J Korean Wood Sci Technol* 2020, **48**: 618–630.
[18] Yao LH, Ji LN, Sun DL, *et al.* Preparation of teakwood bending components with excellent softening properties by vacuum impregnation with triethanolamine compounding solution. *Forests* 2023, **14**: 1773.
[19] Rajendran S, Singh G. *Titanic Corrosion*. Singapore: Jenny Stanford Publishing, 2019.
[20] El-Khouri A, Pellegrino C, Cameron J. Rusticle magnetotaxis elucidating rustflower formations in RMS Titanic's Turkish Baths. *Deep-Sea Res Pt I* 2023, **197**: 104068.
[21] Wan SJ, Li YC, Peng JS, *et al.* Synergistic toughening of graphene oxide-molybdenum disulfide-thermoplastic polyurethane ternary artificial nacre. *ACS Nano* 2015, **9**: 708–714.
[22] Xia S, Wang ZN, Chen H, *et al.* Nanoasperity: Structure origin of nacre-inspired nanocomposites. *ACS Nano* 2015, **9**: 2167–2172.
[23] Zhao CQ, Zhang PC, Zhou JJ, *et al.* Layered nanocomposites by

shear-flow-induced alignment of nanosheets. *Nature* 2020, **580**: 210–215.
[24] Eckert A, Rudolph T, Guo JQ, *et al.* Exceptionally ductile and tough biomimetic artificial nacre with gas barrier function. *Adv Mater* 2018, **30**: 1802477.
[25] Wan SJ, Zhang Q, Zhou XH, *et al.* Fatigue resistant bioinspired composite from synergistic two-dimensional nanocomponents. *ACS Nano* 2017, **11**: 7074–7083.
[26] Liu AD, Walther A, Ikkala O, *et al.* Clay nanopaper with tough cellulose nanofiber matrix for fire retardancy and gas barrier functions. *Biomacromolecules* 2011, **12**: 633–641.
[27] Jin BQ, Wang H, Xu H, *et al.* Bio-inspired nacre-like composites with excellent mechanical properties, gas-barrier function and fire-retardant performances based on self-assembly between hyperbranched poly(amido amine)s and montmorillonite. *RSC Adv* 2023, **13**: 3661–3668.
[28] Tian ZL, Zheng LY, Wang JM, *et al.* Theoretical and experimental determination of the major thermo-mechanical properties of RE_2SiO_5 (RE = Tb, Dy, Ho, Er, Tm, Yb, Lu, and Y) for environmental and thermal barrier coating applications. *J Eur Ceram Soc* 2016, **36**: 189–202.
[29] Zhong X, Wang YW, Niu YR, *et al.* Corrosion behaviors and mechanisms of ytterbium silicate environmental barrier coatings by molten calcium–magnesium–alumino–silicate melts. *Corros Sci* 2021, **191**: 109718.
[30] Ueno S, Ohji T, Lin HT. Recession behavior of $Yb_2Si_2O_7$ phase under high speed steam jet at high temperatures. *Corros Sci* 2008, **50**: 178–182.
[31] Tian ZL, Zhang J, Sun LC, *et al.* Robust hydrophobicity and evaporation inertness of rare-earth monosilicates in hot steam at very high temperature. *J Am Ceram Soc* 2019, **102**: 3076–3080.
[32] Chen L, Yang B, Li GR, *et al.* Thermochemical stability of $Yb_2Si_2O_7$ environmental barrier coatings during thermal cycling and water vapor corrosion at 1350 °C. *J Therm Spray Techn* 2023, **32**: 1811–1827.
[33] Al Nasiri N, Patra N, Horlait D, *et al.* Thermal properties of rare-earth monosilicates for EBC on Si-based ceramic composites. *J Am Ceram Soc* 2016, **99**: 589–596.
[34] Lu MH, Xiang HM, Feng ZH, *et al.* Mechanical and thermal properties of Yb_2SiO_5: A promising material for T/EBCs applications. *J Am Ceram Soc* 2016, **99**: 1404–1411.
[35] Chen GH, Zhang YL, Kong JA, *et al.* Water vapor corrosion behavior of SiC/Si/mixed $Yb_2Si_2O_7$–Yb_2SiO_5 environmental barrier coating for C/C composites. *J Alloys Compd* 2024, **1002**: 175348.
[36] Garcia E, Sotelo-Mazon O, Poblano-Salas CA, *et al.* Characterization of $Yb_2Si_2O_7$–Yb_2SiO_5 composite environmental barrier coatings resultant from *in situ* plasma spray processing. *Ceram Int* 2020, **46**: 21328–21335.
[37] Yu S, Chen GL, Fu JY, *et al.* Yb_2SiO_5–$Yb_2Si_2O_7$ gradient environment barrier coating: Rational design and corrosion behavior in water vapor environment at 1300 °C. *J Eur Ceram Soc* 2024, **44**: 6097–6112.
[38] Zhang JG, Tan X, Fan XJ, *et al.* Thermal insulation performance of 7YSZ TBCs adjusted via Al modification. *Rare Met* 2023, **42**: 994–1004.
[39] Liu MJ, Zhang G, Lu YH, *et al.* Plasma spray–physical vapor deposition toward advanced thermal barrier coatings: A review. *Rare Metals* 2020, **39**: 479–497.
[40] Zhang XF, Li M, Zhang A, *et al.* Al-modification for PS-PVD 7YSZ TBCs to improve particle erosion and thermal cycle performances. *J Adv Ceram* 2022, **11**: 1093–1103.
[41] Wu J, Yang WC, Zhang XF, *et al.* Corrosion behavior of PS-PVD spray $Yb_2Si_2O_7$ environmental barrier coatings during continuous water vapor exposure. *Corros Sci* 2023, **210**: 110831.
[42] Richards BT, Zhao HB, Wadley HNG. Structure, composition, and defect control during plasma spray deposition of ytterbium silicate coatings. *J Mater Sci* 2015, **50**: 7939–7957.
[43] Wang HY, Luo ZX, Sun LC, *et al.* Comprehensive microstructural characterization and CMAS infiltration resistance of ytterbium disilicate coatings with lamellar and quasi-columnar structures. *Corros Sci* 2023, **221**: 111316.
[44] Huang JQ, Liu RY, Hu Q, *et al.* Effect of deposition temperature on phase composition, morphology and mechanical properties of plasma-sprayed $Yb_2Si_2O_7$ coating. *J Eur Ceram Soc* 2021, **41**: 7902–7909.
[45] Huang SJ, Ali AN. Effects of heat treatment on the microstructure and microplastic deformation behavior of SiC particles reinforced AZ61 magnesium metal matrix composite. *Mat Sci Eng A-Struct* 2018, **711**: 670–682.
[46] Wang HY, Zhang J, Sun LC, *et al.* Microstructure and phase composition evolution of dual-phase ytterbium silicate coatings plasma sprayed from stoichiometric $Yb_2Si_2O_7$ feedstock powder. *Surf Coat Tech* 2022, **437**: 128373.
[47] Sampath S, Herman H. Rapid solidification and microstructure development during plasma spray deposition. *J Therm Spray Techn* 1996, **5**: 445–456.
[48] Garcia E, Lee H, Sampath S. Phase and microstructure evolution in plasma sprayed $Yb_2Si_2O_7$ coatings. *J Eur Ceram Soc* 2019, **39**: 1477–1486.
[49] Bakan E, Marcano D, Zhou DP, *et al.* $Yb_2Si_2O_7$ environmental barrier coatings deposited by various thermal spray techniques: A preliminary comparative study. *J Therm Spray Techn* 2017, **26**: 1011–1024.
[50] Wang CJ, Wang Y. Crystal growth behavior and sintering-resistance property of nano-sized β-$Yb_2Si_2O_7$ for environmental barrier coatings. *Ceram Int* 2020, **46**: 19514–19518.
[51] Yang GJ, Li CX, Hao S, *et al.* Critical bonding temperature for the splat bonding formation during plasma spraying of ceramic materials. *Surf Coat Tech* 2013, **235**: 841–847.
[52] Cipitria A, Golosnoy IO, Clyne TW. A sintering model for plasma-sprayed zirconia TBCs. Part I: Free-standing coatings. *Acta Mater* 2009, **57**: 980–992.
[53] Lv BW, Zhuo XS, Wang C, *et al.* Mechanisms of crack healing in dense Yb–Si–O environmental barrier coatings by plasma spray-physical vapor deposition. *Ceram Int* 2022, **48**: 15975–15983.
[54] Zhang XF, Zhou KS, Deng CM, *et al.* Gas-deposition mechanisms of 7YSZ coating based on plasma spray-physical vapor deposition. *J Eur Ceram Soc* 2016, **36**: 697–703.